Linking Glacial-Interglacial states to multiple equilibria of climate

David Ferreira[1*], John Marshall[2], Takamitsu Ito[3] & David McGee[2]

[1]*Department of Meteorology, University of Reading*

[2]*Department of Earth, Atmospheric and Planetary Sciences, Massachusetts Institute of Technology*

[3]*School of Earth and Atmospheric Sciences, Georgia Tech*

Glacial-Interglacial cycles (GIC) are often described as an amplified global response of the climate to perturbations in solar radiation caused by oscillations of Earth's orbit. However, it remains unclear whether internal feedbacks are large enough to account for the radically different Glacial and Interglacial states. Here we provide support for an alternative view: Glacial-Interglacial states are multiple equilibria of the climate system which exist for the same external forcing. It is the nature of these equilibrium states, rather than the forcing and feedbacks, that sets the amplitude of the cycles. We show here that such multiple equilibria resembling Glacial and Interglacial states can be found in a complex coupled General Circulation Model of the ocean-atmosphere-sea ice system. The multiple states are sustained by ice-albedo feedback modified by ocean heat transport and are not related to the bi-stability of the ocean's meridional overturning circulation. In addition, the dynamical shifts between the states can drive a 100 ppm pCO_2 change, close to that seen in ice cores, a consequence of the Southern Hemisphere ice pack expansion/contraction over regions of upwelling regulating outgassing of CO_2 to the atmo-

sphere.

The link between GIC and variations of Earth's orbital parameters (Milankovitch cycles) is central to our understanding of ice ages[1–3]. However, there is no generally accepted mechanism by which the Milankovitch cycles pace the GIC[4]. A puzzling aspect of the astronomical hypothesis is that small global insolation fluctuations must drive large global shifts of the climate system. This is typically addressed by invoking either strong internal feedbacks or some non-linear mechanism. If strong internal feedbacks are at play, land/sea ice-albedo feedbacks (combined with large local insolation changes) and CO_2 feedbacks are most likely. This behavior has been encapsulated in conceptual models[5,6], but as yet there is no example of a GCM simulating GICs when solely forced with Milankovitch cycles, in the absence of prescribe feedbacks such as land-ice and CO_2 changes.

Taking a non-linear perspective, various studies have explored the possibility of free oscillations of the climate system, paced or phased-locked by the Milankovitch forcing[7–9]. Others[10–12] hypothesized that the Glacial and Interglacial states are two possible equilibrium states of Earth's climate. In this case, the Milankovitch radiative forcing provides the small kicks necessary for the climate system to exceed thresholds and transition between states. Multiple equilibrium states are commonly found in low-order or conceptual climate models. The Budyko-Sellers type of models are a well known example, which possess multiple equilibria through sea-ice albedo feedback[13,14]. However, it is unclear whether more complex systems, and ultimately Earth's climate, can sustain multiple equilibrium states on the global scale and of a magnitude pertaining to GIC. We show here that they can.

Modeling context. Simulations are carried out with the MIT GCM[15] which solves for the three-dimensional circulation of atmosphere and ocean, and includes sea ice, biogeochemical cycling and land surface processes (see SI for details). The configuration comprises two 45°-wide land masses defining a narrow Atlantic-like basin and a wide Pacific-like basin connecting to an unblocked southern ocean (Fig. 1). Despite an idealized geometry, the model includes very many degrees of freedom and captures many of the essential dynamics (e.g. atmospheric storm tracks and hydrological cycle, gyres and circumpolar current in the oceans, and a sea ice cycle) that shape Earth's climate system[16–19].

Two stable equilibria of climate are supported, one "Cold" and one "Warm" for the same external forcing and parameters, thus demonstrating that multiple equilibria are possible in a coupled GCM comprising a myriad degrees of freedom. The difference in the climate of the two states is of planetary scale. Global average sea surface temperature and surface air temperature differ by 8.2°C and 13.5°C, respectively [patterns are shown in Fig. S1]. In the Southern Hemisphere (SH), the sea ice edge (as measured by the 15% annual mean concentration) expands by about 15° of latitude in the Cold state (Fig. 1). The Northern Hemisphere, which is nearly ice-free in the Warm state, exhibits a large ice cap extending over the subpolar gyre (45°N) in the Cold state, with a similar expansion of snow cover over land (Fig. 1, top left).

Previous thinking about past climate changes has been dominated by the idea that the Atlantic meridional overturning circulation (AMOC) may be "on" or "off". This bi-stability is primarily an oceanic process[20] with weak climate imprint outside of the North Atlantic basin[21,22]. Despite numerous caveats[23,24], it is often invoked to explain abrupt climate changes such as

Dansgaard-Oeschger and Heinrich events. The multiple states described here differ fundamentally from the AMOC bi-stability by their coupled nature (see below). Moreover, they are associated with climate shifts of global extent comparable to those observed in the past, providing a novel framework to interpret Glacial and Interglacial states.

Previous studies of the aquaplanet[14,25,26] have revealed that multiple states of the kind shown in Fig. 1 owe their existence to a fundamental and robust feature of the ocean circulation: the ocean heat transport (OHT) peaks near 15-20°N/S and drops sharply in the mid-latitudes (Fig. 2, top right). This reflects the presence on both sides of the Equator of shallow (0-400 m) wind-driven overturning cells associated with the trade winds (Fig. 3) which transport warm surface waters from the Equator into middle latitudes. The pronounced OHT convergence in the subtropics can arrest a runaway expansion of sea ice through the ice-albedo feedback and permits the existence of a steady state with a large ice cap encroaching down into mid-latitudes. Another equilibrium state is possible with nearly ice-free conditions, in which ice albedo feedback promoting the sea ice expansion is weak and easily balanced by the ocean and atmosphere heat transport to the poles. The large ice cap state is unstable in the classic Budyko-Sellers model but stabilized in our GCM by the structure of OHT. This is formalized in a modified Budyko-Sellers-type model[14,25] which predicts a stable ice edge on the poleward side of the peak OHT, consistent with our GCM simulations (Fig. 2, top right and Fig. S2).

Circulation patterns in Warm and Cold states. As expected, the Cold state exhibits a weaker hydrological cycle than the Warm state, as illustrated by the smaller amplitude of the evaporation minus precipitation field (Fig. 2), consistent with the "dry gets drier and wet gets wetter" principle seen in global warming experiments[27]. The SH jet stream weakens slightly (by $\sim$10%) and shifts northward (by 1.5° lat) in the Cold state, reflecting a northward displacement of the baroclinic zone (strong surface temperature gradient) following the sea ice expansion (further details on the atmospheric states in Fig. S3).

Differences between equilibrium states are also pronounced in the deep ocean. The Cold state has an intensified bottom cell (10 Sv cf 3 Sv of Warm state) emanating from the south (Fig. 3, left). These waters, analogous to the Antarctic Bottom Water (AABW) of the present-day ocean, are produced by brine rejection in the regions of production and export of sea ice. As the southern source is stronger in the Cold state, bottom waters approach the freezing point everywhere (~ -1.5°C from 7°C in the Warm state) and become saltier by $\sim$0.5 psu. In contrast, the upper overturning cell (above $\sim$2000 m) is weaker in the Cold state by 5 Sv (Fig. 3). This is not the result of a change in the SH westerly winds and associated upwelling rates. Rather, it is the consequence of a shift in the partitioning of upwelled water between the upper and lower cells: while upwelling mainly feeds the upper cell in the Warm state, upwelled waters are equally partitioned between the upper and lower cells in the Cold state.

The re-organization of the global overturning reflects changes in SH surface buoyancy fluxes, consistent with the conceptual model of Watson et al.[28,29]. In steady state, poleward (equatorward) flowing surface waters must lose (gain) buoyancy to (from) the atmosphere and sea ice[30,31]. Within the ice pack, the ocean experiences net buoyancy loss as freezing and brine rejection dominate exchanges. A transition to net buoyancy gain occurs in the seasonal ice zone, where melting due to exported sea ice dominates. As the sea ice advances in the Cold state, the region of buoyancy loss expands northward (from 70 to 50°S) into the region of wind-driven upwelling, drawing a larger fraction of the upwelled water into the lower cell.

In the small (Atlantic-like) basin (Fig. 3, right), the Cold state is associated with a weaker (but not collapsed) upper cell (from 20 to 12 Sv), a shoaling of the dense water return flow, a southward shift of deep convection following the ice margin, and a stronger bottom cell fed from the south (see Fig. S4 for the large basin overturning). The large increase in sea ice cover seals off the polar ocean and strongly suppresses air-sea buoyancy flux.

Re-organization of the deep circulation between the two states has a profound impact on the distribution of tracers, as illustrated by the phosphate distribution (Fig. 3, right). The nutrient load is dramatically enhanced in the deep ocean of the Cold state relative to the Warm state. While nutrient-depleted waters are only found in the top 300 m in the Warm state, they extend to 2000 m in the Cold state where nutrients accumulate in the bottom cell and remain confined below 2000 m outside of the Southern Ocean.

Atmospheric pCO_2 and biogeochemistry. A fascinating characteristic of the two equilibria is that the atmospheric CO_2 content is significantly lower in the Cold state (157 ppm) than in the Warm state (268 ppm). Both climate states contain the same carbon, phosphate and alkalinity inventories: the atmospheric CO_2 variation is an emergent property of the climate-carbon system resulting from the multiple equilibrium states (it does not feed back on the radiative balance of the atmosphere and the multiple equilibria of the physical system are unaffected).

A decomposition of the oceanic carbon reservoir[32] is used to diagnose the relative roles of different carbon pump components (see SI for details). The increased ocean carbon storage in the Cold state is primarily due to the increased air-sea disequilibrium pump (C_{dis}), which is reinforced by a cooling-induced solubility increase and partially compensated by the weakened biological carbon storage (Table 1).

In the Warm state, C_{dis} is near neutral (a global mean of +4.3 μmol kg^{-1}) consistent with the modern climatology (Fig. 3, left), where the upper cell is weakly undersaturated ($C_{dis} < 0$) and the lower cell weakly supersaturated ($C_{dis} > 0$). In the Cold state, C_{dis} becomes strongly supersaturated, equivalent to an atmospheric CO_2 drawdown of -87 ppm. The increased C_{dis} is evident in the AABW-like waters that originate in the SH (Fig. 3, bottom left). This is driven by the expansion of the sea ice over the area of upwelling, limiting the outgassing of CO_2 from the upwelled DIC-rich waters. This mechanism was first postulated by *Stephens and Keeling*[33] using a simple box model in which sea ice cover is prescribed. This idea has been challenged arguing that the seasonal cycle of sea ice cover can expose a significant fraction of the upwelling regions to air-sea equilibration through melting and opening of the sea ice. Our calculation explicitly represents the seasonal cycle of sea ice cover and its impact on the air-sea gas transfer. Moreover, the modeled Warm state successfully reproduces the observed distribution of modern C_{dis}[32]. Our simulations thus lend strong support for such a mechanism provided that the sea ice expansion reaches into the Southern Ocean upwelling region. It is likely that the reorganization of the MOC also contributes significantly, as a larger fraction of the upwelled water in the Southern Ocean is transported southward under the Cold state.

It should be noted that our model overestimates the solubility-driven CO_2 drawdown (-

58 ppm) because of the large decline in the mean ocean temperature (-7.7°C). For a realistic ocean cooling (2-4°C), we estimate it would be -23±8 ppm, reducing the total CO_2 drawdown to -71±7 ppm.

The biological carbon storage is reduced in the Cold state, primarily due to the reorganization of the deep circulation and the dominance of AABW-like water with an elevated preformed phosphorus. In contrast, the surface phosphate is strongly depleted in the ice-free regions of the SH, leading to the decline in the phosphate inventory of the upper overturning cell. The expansion of sea ice in the Cold state weakens the biological productivity in the high-latitude Antarctic waters, consistent with paleo-productivity proxies[34,35]. Combining the effects of organic and carbonate pumps (see SI), the net biological pump increases the atmospheric CO_2 by +36 ppm. The role of the biological carbon pump is the most uncertain aspect of our study. In particular our model does not reproduce the elevated glacial productivity in the Subantarctic latitudes, perhaps due to the lack of iron cycling[34].

Despite this limitation, our model reproduces several important features of glacial carbon cycling. Phosphate accumulates in the deep water and is depleted in the upper water column (Fig. 3), consistent with nutrient proxies [36,37]. While Antarctic preformed nutrient concentrations are relatively high in our model, the deep water still contains a high level of DIC in the lower limb of the MOC due to the elevated level of C_{dis}. This allows the retention of excess DIC in the bottom water while avoiding the widespread anoxia which would occur if the carbon sequestration were dominated by C_{org}.

Comparing to the observed Glacial and Interglacial states. Differences between our

Warm and Cold states show striking similarities with inferred differences between the present climate and that of the LGM (Fig. 4).

Reconstruction of the Southern Ocean sea ice edge for the LGM indicates an equatorward displacement in the wintertime ranging between 7 and 10° of latitude relative to present time[38], which compares favorably with our simulated ice expansion (13° of latitude). Estimates for the summertime LGM are more uncertain but suggest a patchy expansion with large values in the Weddell sector (up to 15° of latitude) and no change in the Indian sector (the sea ice retreating almost back to the coast as today). Our model cannot capture these asymmetries and is likely most relevant to the Weddell sector where the coast is much further south. There, the estimated (15°) and simulated (18°) wintertime changes are of the same magnitude.

Although the strength and position of the SH westerly winds in the glacial periods has received much attention as a possible driver of the atmospheric CO_2 change[39], paleoproxy data are very uncertain[40,41] while simulations of the LGM show very little agreement among models[42]. In our simulations, changes in the SH jet stream (Fig. 2) have little impact on CO_2 which is mainly driven by changes in sea ice cover.

In the North Atlantic, paleoproxies suggest that the LGM wintertime sea ice cover was greatly expanded, likely covering the Nordic Seas and most of the subpolar gyre[43] and possibly down to the British Isles during stadial conditions[44]. Reconstructions also suggest a southwest-northeast tilted ice edge along the path of the North Atlantic drift, as seen in our model.

The large shift in deep ocean nutrients between the Warm and Cold states (Fig. 3, left) is consistent with estimates for the present-day and LGM[45]. Estimates of the equivalent $\delta^{13}C$ distributions for the two states are shown in SI, Fig. S5. There is a striking similarity between the reconstructed $\delta^{13}C$ distribution from the simulation and maps for the LGM[46]. These rearrangements of the tracer distributions (e.g. $\delta^{13}C$) have been interpreted as reflecting a slightly weaker and shallower AMOC at the LGM[46–48]. Although such interpretations should be taken with caution[49], we do observe a consistent set of changes in circulation/tracer patterns that parallels those inferred for the LGM.

Bottom waters at the LGM are estimated to be near the freezing point at all latitudes and saltier than today by 1 and 2.4 psu[50]. Similar tendencies are seen in our simulations although bottom salinity only increases by +0.5 psu in the Southern Ocean, decreasing to zero at the North pole. As our model does not allow large accumulation of freshwater over land (we do not have ice sheets), the modeled salinity shifts provides an estimate of the contribution of ocean circulation changes and increased brine rejection to the observed change.

It is apparent that the temperature difference between the two states is larger than inferred for the LGM-present difference. This is traceable to a warm bias in Northern surface temperatures of the Warm state which is communicated to the global ocean through deep water formation (at $\sim$7°C compared to $\sim$3°C for the present day). This could be due to our idealized land distributions that facilitates OHT toward high latitudes, and/or the narrow width of the continent that limits the advection of cold dry air over the oceans.

Conclusions. We have shown that multiple equilibria of global scale are possible in a complex coupled GCM with an Earth-like geometry. The robust dynamics that enables such states (a large heat release from the ocean to the atmosphere in mid-latitudes[14,25]) suggests that they could exist in Earth's climate. Striking similarities (both in terms of circulation and biogeochemical signatures) between our two climate states and that of the LGM/present-day suggest that GIC could be facilitated by the existence of multiple equilibria. If confirmed, this would have a profound impact on our interpretation of the paleo-record, notably of the relationship between the Milankovitch cycles and the observed response. For example, multiple equilibria may help to explain the surprising similarity of GIC's amplitudes despite highly variable magnitudes of insolation change during glacial terminations. Although here we emphasize the link with the GIC, our findings may also be relevant to the shorter (millennial) climate variability, such as Dansgaard-Oeschger and Heinrich events. Perhaps DO-like fluctuations could be interpreted as failed transitions from the Cold to the Warm states.

Future work should test whether these states persist in the presence of improved physics (notably land ice[51] and radiative CO_2 feedbacks) and of a realistic geometry. We feel that the search for such equilibria in climate models has been neglected and should be more systematic.

Acknowledgements JM would like to acknowledge support from NSF and NOAA.

Competing Interests The authors declare that they have no competing financial interests.

Correspondence Correspondence and requests for materials should be addressed to D.F. (email: d.g.ferreira@reading.ac.ul

Authors contributions DF and JM designed and analyzed the experiments. TK lead the carbon cycle analysis. DM provided expertise for the paleoclimate comparison. All authors contributed to the writing of the paper.

1. Hays, J. D., Imbrie, J. & Shackleton, N. J. Variations in the earth's orbit: Pacemaker of the ice ages. *Science* **194**, 1121–1132 (1976).

2. Raymo, M. E., Lisiecki, L. E. & Nisancioglu, K. H. Plio-pleistocene ice volume, Antarctic climate, and the global δ^{18}O record. *Science* **313**, 492–495 (2006).

3. Huybers, P. Combined obliquity and precession pacing of late pleistocene deglaciations. *Nature* **480**, 229–232 (2011).

4. Paillard, D. Quaternary glaciations: from observations to theories. *Quat. Sci. Rev.* **107**, 11–24 (2015).

5. Imbrie, J. & Imbrie, J. Z. Modeling the climatic response to orbital variations. *Science* **207**, 943–953 (1980).

6. Parrenin, F. & Paillard, D. Amplitude and phase of glacial cycles from a conceptual model. *Earth and Planet. Sci. Lett.* **214**, 243–250 (2003).

7. Saltzman, B., Hansen, A. R. & Maasch, K. A. The late quaternary glaciatiosn as the response of a three-component feedback system to the earth-orbital forcing. *J. Atmos. Sci.* **41**, 3380–3389 (1984).

8. Le Treut, H. & Ghil, M. Orbital forcing, climatic interactions, and glaciation cycles. *J. Geophys. Res.* **88**, 5167–5190 (1983).

9. Gildor, H. & Tziperman, E. Sea ice as the galical cycles's climate switch: Role of seasonal and orbital forcing. *Paleoceanography* **15**, 605–615 (2000).

10. Nicolis, C. Stochastic aspects of climatic transitions – response to a periodic forcing. *Tellus* **34**, 1–9 (1982).

11. Benzi, R., Parisi, G., Sutera, A. & Vulpiani, A. Stochastic resonance in climatic change. *Tellus* **34**, 10–16 (1982).

12. Paillard, D. The timing of pleistocene glaciations from a simple multiple-state climate model. *Nature* **391**, 378–381 (1998).

13. North, G. R., Cahalan, R. F. & Jr, J. A. C. Energy balance climate models. *Rev. Geophysics and Space Physics* **19**, 91–121 (1981).

14. Rose, B. E. & Marshall, J. Ocean Heat Transport, sea ice and multiple climatic states: Insights from Energy Balance Models. *J. Atmos. Sci.* **66**, 2828–2843 (2009).

15. Marshall, J., Adcroft, A., Hill, C., Perelman, L. & Heisey, C. A finite-volume, incompressible navier stokes model for studies of the ocean on parallel computers. *J. Geophys. Res.* **102**, 5753–5766 (1997).

16. Marshall, J., Ferreira, D., Campin, J. & Enderton, D. Mean climate and variability of the atmosphere and ocean on an aquaplanet. *J. Atmos. Sci.* **64**, 4270–4286 (2007).

17. Enderton, D. & Marshall, J. Explorations of atmosphere-ocean-ice climates on an aquaplanet and their meridional energy transports. *J. Atmos. Sci.* **66**, 1593–1611 (2009).

18. Ferreira, D., Marshall, J. & Campin, J.-M. Localization of deep water formation: role of atmospheric moisture transport and geometrical constraints on ocean circulation. *J. Climate* **23**, 1456–1476 (2010).

19. Marshall, J., Donohoe, A., Ferreira, D. & McGee, D. The ocean's role in setting the mean position of the atmosphere's itcz. *Climate Dyn.* (2013).

20. Stommel, H. Thermohaline convection with two stable regimes of flow. *Tellus* **13**, 224–230 (1961).

21. Manabe, S. & Stouffer, R. J. Two stable equilibria of a coupled ocean-atmosphere model. *J. Climate* **1**, 841–866 (1988).

22. Vellinga, M. & Wood, R. Global climatic impacts of a collapse of the atlantic thermohaline circulation. *Climate Change* **54**, 251–267 (2002).

23. Wunsch, C. *Ocean Circulation: Mechanisms and Impacts - Past and Future Changes of Meridional Overturning*, chap. The past and future ocean circulation from a contemporary perspective (American Geophysical Union, Washington, DC, 2007).

24. Seager, R. & Battisti, D. S. *The Global Circulation of the Atmosphere*, chap. Challenges to Our Understanding of the General Circulation: Abrupt Climate Change (Princeton University Press, 2007).

25. Ferreira, D., Marshall, J. & Rose, B. Climate determinism revisited: multiple equilibria in a complex climate model. *J. Climate* **24**, 992–1012 (2011).

26. Rose, B., Ferreira, D. & Marshall, J. The role of oceans and sea ice in abrupt transitions between multiple climate states. *J. Climate* **26**, 2862–2879 (2013).

27. Held, I. & Soden, B. J. Robust responses of the hydrological cycle to global warming. *J. Climate* **19**, 5686–5699 (2006).

28. Watson, A. J., Vallis, G. K. & Nikurashin, M. Southern ocean buoyancy forcing of ocean ventilation and glacial atmospheric CO_2. *Nature Geoscience* **8**, 861–864 (2015).

29. Ferrari, R. *et al.* Antarctic sea ice control on ocean circulation in present and glacial climates. *Proc. Natl. Acad. Sci.* **111**, 8753–8758 (2014).

30. Marshall, D. Subduction of water masses in an eddying ocean. *J. Mar. Res.* **55**, 201–222 (1997).

31. Marshall, J. & Radko, T. Residual mean solutions for the antarctic circumpolar current and its associated overturning circulation. *J. Phys. Oceanogr.* **33**, 2341–2354 (2003).

32. Ito, T. & Follows, M. J. Air-sea disequilibrium of carbon dioxide enhances the biological carbon sequestration in the southern ocean. *Glob. Biogeochem. Cy.* **27**, 1–10 (2013).

33. Stephens, B. B. & Keeling, R. F. The influence of antarctic sea ice on glacial-interglacial CO_2 variations. *Nature* **404**, 171–174 (2000).

34. Kohfeld, K. E., Le Quéré, C., Harrison, S. P. & Anderson, R. F. Role of marine biology in glacial-interglacial co2 cycles. *Science* **308**, 74–78 (2005).

35. Jaccard, S. L. *et al.* Two modes of change in southern ocean productivity over the past million years. *Science* **339**, 1419–1423 (2013).

36. Boyle, E. A. Vertical oceanic nutrient fractionation and glacial/interglacial co2 cycles. *Nature* **331**, 55–56 (1988).

37. Jaccard, S. L. *et al.* Subarctic pacific evidence for a glacial deepening of the oceanic respired carbon pool. *Earth and Planet. Sci. Lett.* **277**, 156–165 (2009).

38. Gersonde, R., Crosta, X., Abelmann, A. & Armand, L. Sea-surface temperature and sea ice distribution of the southern ocean at the epilog last glacial maximum—a circum-antarctic view based on siliceous microfossil records. *Quat. Sci. Rev.* **24**, 869–896 (2005).

39. Toggweiler, J. R. Shifting westerlies. *Science* **323**, 1434–1435 (2009).

40. Kohfeld, K. E. *et al.* Southern hemisphere westerly wind changes during the last glacial maximum: paleo-data synthesis. *Quat. Sci. Rev.* **68**, 76–95 (2013).

41. Shulmeister, J. *et al.* The southern hemisphere westerlies in the australasian sector over the last glacial cycle: a synthesis. *Quat. Int.* **118**, 23–53 (2004).

42. Sime, L. C. *et al.* Sea ice led to poleward-shifted winds at the last glacial maximum: the influence of state dependency on CMIP5 and PMIP3 models. *Clim. Past Discuss.* **12**, 2241–2253 (2016).

43. de Vernal, A. *et al.* Reconstruction of sea-surface conditions at middle to high latitudes of the northern hemisphere during the last glacial maximum (LGM) based on dinoflagellate cyst assemblages. *Quat. Sci. Rev.* **24**, 897–924 (2005).

44. Dokken, T., Nisancioglu, K. H., Li, C. & Battisti, D. Dansgaard-oeschger cycles: Interactions between ocean and sea ice intrinsic to the nordic seas. *Paleoceanography* **28**, 491–502 (2013).

45. Boyle, E. A. & Keigwin, L. D. Comparison of atlantic and pacific paleochemical records for the last 215,000 years: changes in deep ocean circulation and chemical inventories. *Earth and Planet. Sci. Lett.* **76**, 135–150 (1985).

46. Curry, W. B. & Oppo, D. W. Glacial water mass geometry and the distribution of δ^{13}C of CO_2 in the western atlantic ocean. *Paleoceanography* **24**, PA1017 (2005).

47. Lynch-Stieglitz, J. *et al.* Atlantic meridional overturning circulation during the last glacial maximum. *Science* **316**, 66–69 (2007).

48. Peterson, C. D., Lisiecki, L. E. & Stern, J. V. Deglacial whole-ocean ^{13}c change estimated from 480 benthic foraminiferal records. *Paleoceanography* **29**, 549–563 (2014).

49. Gebbie, G. How much did glacial north atlantic water shoal? *Paleoceanography* **29**, 190–209 (2014).

50. Adkins, J. F., McIntyre, K. & Schrag, D. The salinity, temperature and δ^{18}O of the glacial deep ocean. *Science* **298**, 1769–1773 (2002).

51. Abe-Ouchi, A. *et al.* Insolation-driven 100,000-year glacial cycles and hysteresis of ice-sheet volume. *Nature* **500**, 190–194 (2013).

Figure 1 Temperature and ice distributions in the two equilibrium states. Sea Surface Temperature (blue-red shading, in $^\circ$C) and sea ice thickness (white-brown shading, in meter) for the (left) Cold and (right) Warm states. Over the continents, the Surface Air Temperature and snow depth are shown instead. The thick solid line denotes the continental boundaries. The barotropic streamfunction for the ocean is shown in black contours (solid for clockwise, dashed for counter clockwise). Both states are obtained for the same external forcing and same parameters.

Figure 2 Energy transport and hydrological cycle. Surface zonal wind stress (N/m^2, top left), evaporation minus precipitation (mm/day, bottom left) and the net energy transports (in PW =10^{15} W) in the ocean (top right) and atmosphere (bottom, right). The Warm and Cold states are denoted by red and blue lines, respectively. Horizontal arrows indicate the sea ice extent (15% sea ice fraction) where the length of the arrowheads denote the minimum/maximum seasonal range.

Figure 3 Meridional Overturning circulation and carbon cycle. (left) Global overturning circulation (in Sv, black lines) overlaid on the global disequilibrium reservoir C_{dis} (shading, in μmol/kg; zero contour highlighted with a thick white line). (Right) small basin overturning circulation overlaid on phosphate concentration (in μmol kg^{-1}). For the overturning, solid and dashed lines denote clockwise and counter-clockwise circulations, respectively. The Warm state is shown in the top row and the Cold state in the bottom row.

Figure 4 Comparison of observations and simulations. Observed changes between the LGM and present-day climates from observations (red arrows) along with the corresponding differences between the Cold and Warm states of our idealized Earth-like climate simulations (blue arrows). When possible, arrows are scaled to represent the magnitude of the changes. Double arrows for observation gives the range of uncertainties.

	Solubility		Organic	Carbonate		Disequilibrium	net
	δC_{sat}^{T}	δC_{sat}^{S}	δC_{org}	δC_{CaCO3}	δC_{sat}^{A}	δC_{dis}	
δC, μmol/kg	56.4	-0.1	-50.9	-24.2	39.6	+85.3	+106.1
δCO_2, ppm	-57.8	0.1	52.2	24.8	-40.6	-87.5	-108.8

Table 1: Carbon reservoir changes between the Warm and Cold states of the model. δC refers to the dissolved inorganic carbon concentration in the ocean, while δCO_2 refers to the mixing ratio of carbon dioxide in the atmosphere. See Supplementary Information for explanation of the different carbon pumps.

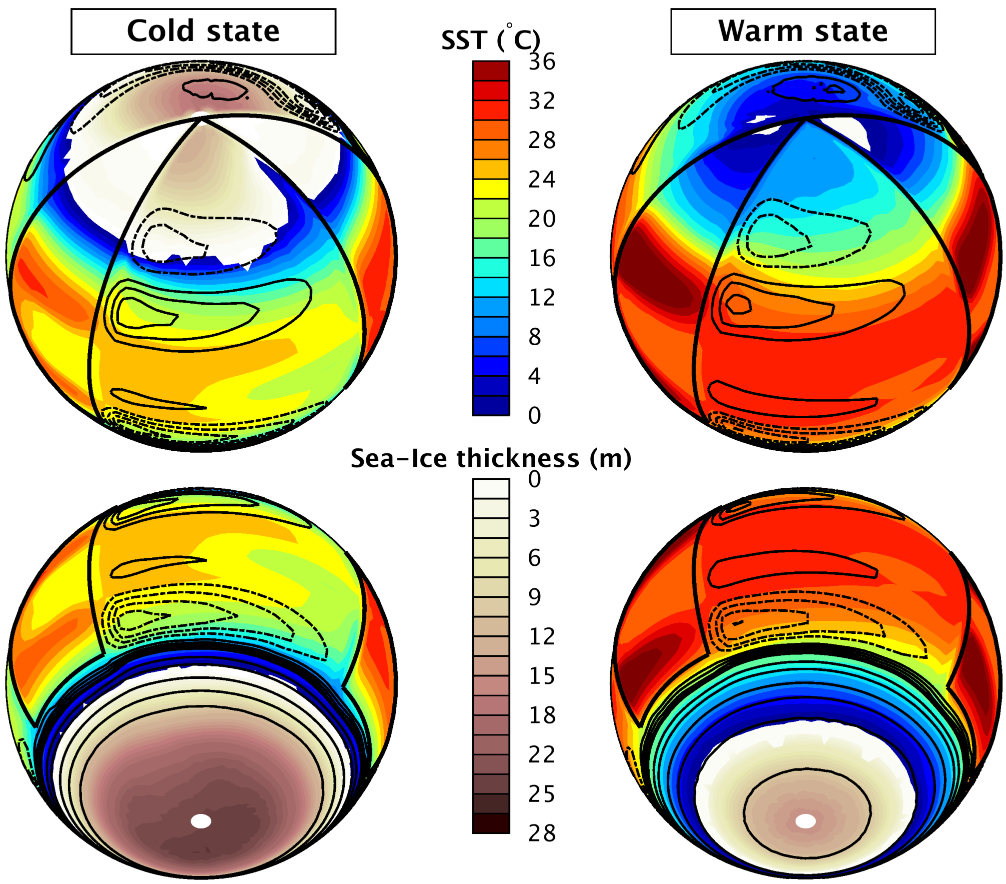

Figure 1: **Temperature and ice distributions in the two equilibrium states.** Sea Surface Temperature (blue-red shading, in °C) and sea ice thickness (white-brown shading, in meter) for the (left) Cold and (right) Warm states. Over the continents, the Surface Air Temperature and snow depth are shown instead. The thick solid line denotes the continental boundaries. The barotropic streamfunction for the ocean is shown in black contours (solid for clockwise, dashed for counter clockwise). Both states are obtained for the same external forcing and same parameters.

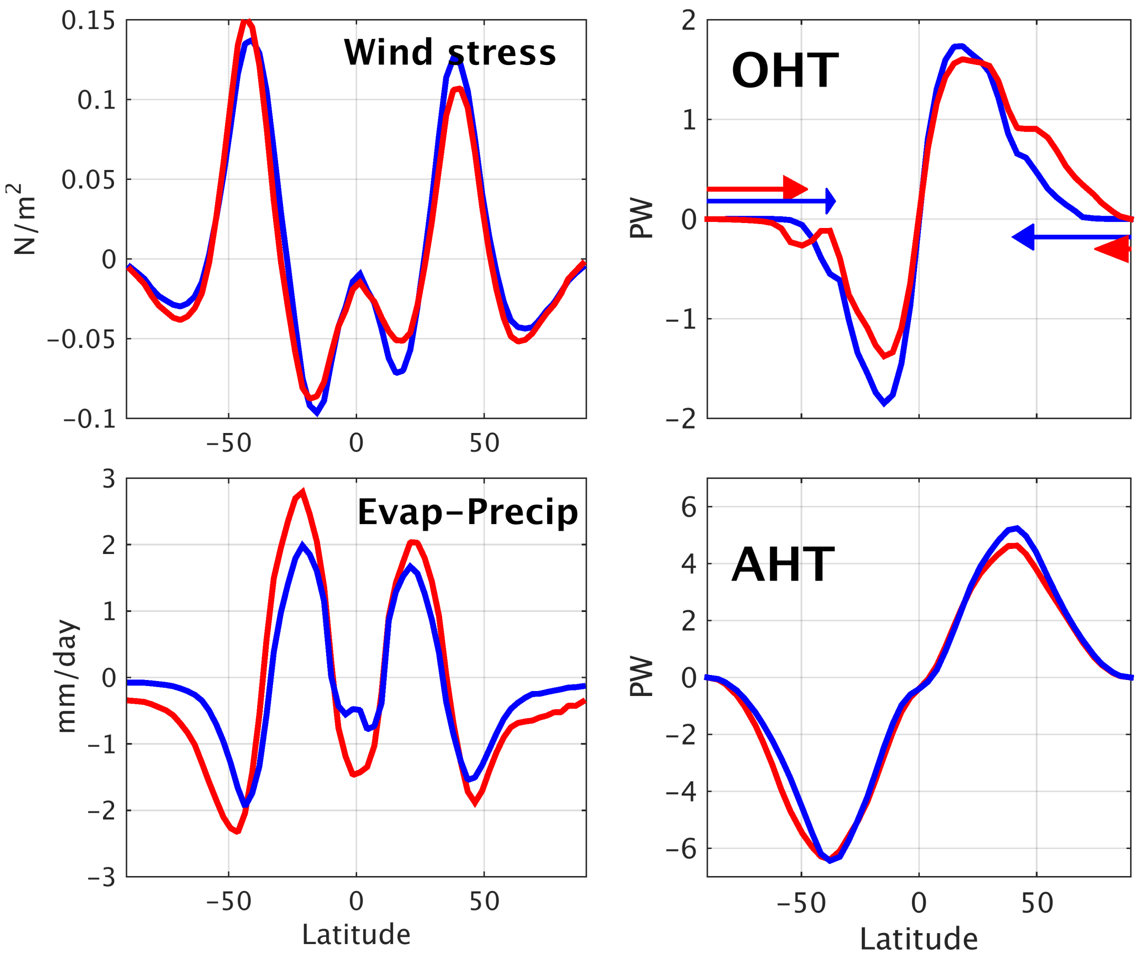

Figure 2: **Energy transport and hydrological cycle.** Surface zonal wind stress (N/m^2, top left), evaporation minus precipitation (mm/day, bottom left) and the net energy transports (in PW $=10^{15}$ W) in the ocean (top right) and atmosphere (bottom, right). The Warm and Cold states are denoted by red and blue lines, respectively. Horizontal arrows indicate the sea ice extent (15% sea ice fraction) where the length of the arrowheads denote the minimum/maximum seasonal range.

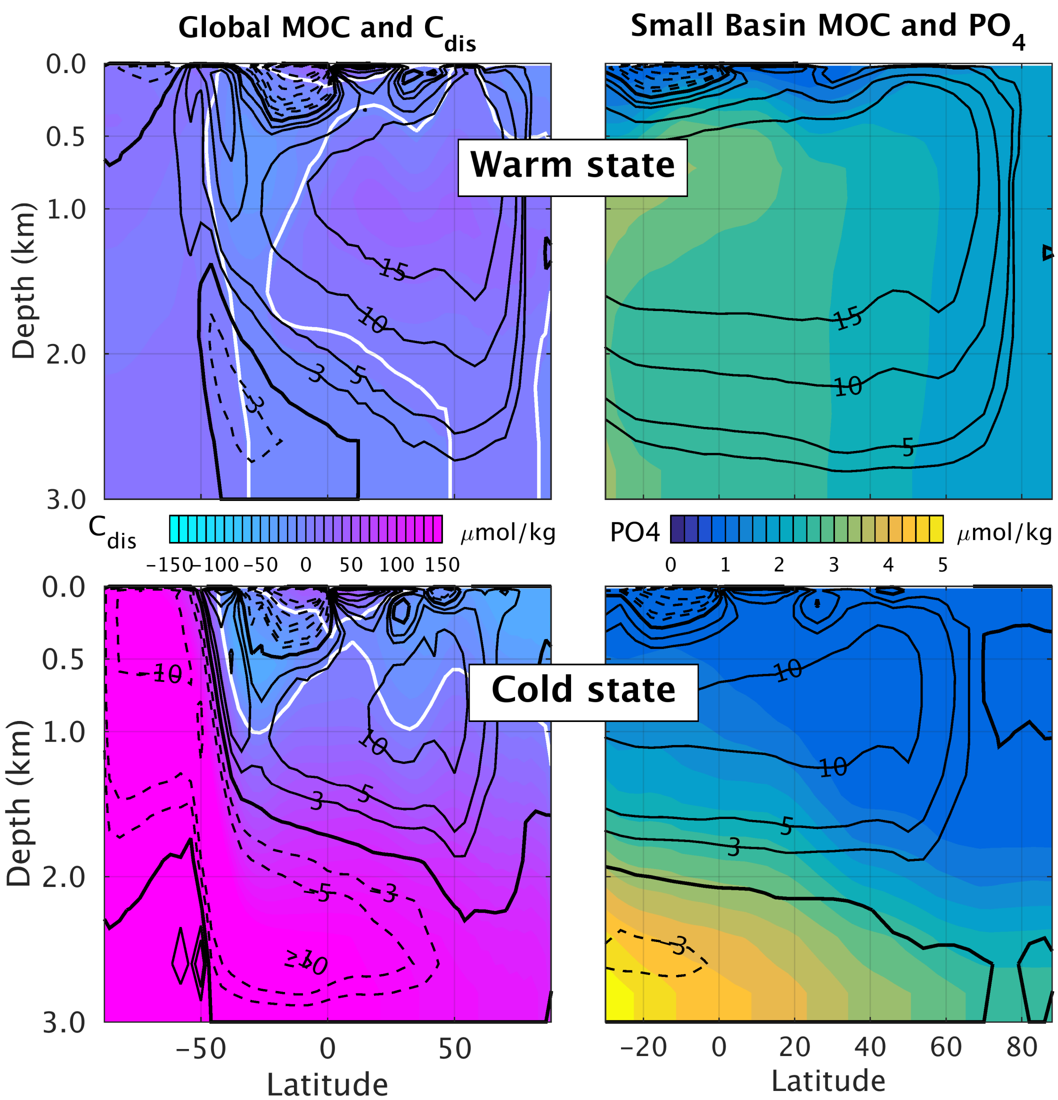

Figure 3: **Meridional Overturning circulation and carbon cycle.** (left) Global overturning circulation (in Sv, black lines) overlaid on the global disequilibrium reservoir C_{dis} (shading, in μmol/kg; zero contour highlighted with a thick white line). (Right) small basin overturning circulation overlaid on phosphate concentration (in μmol kg^{-1}). For the overturning, solid and dashed lines denote clockwise and counter-clockwise circulations, respectively. The Warm state is shown in the top row and the Cold state in the bottom row.

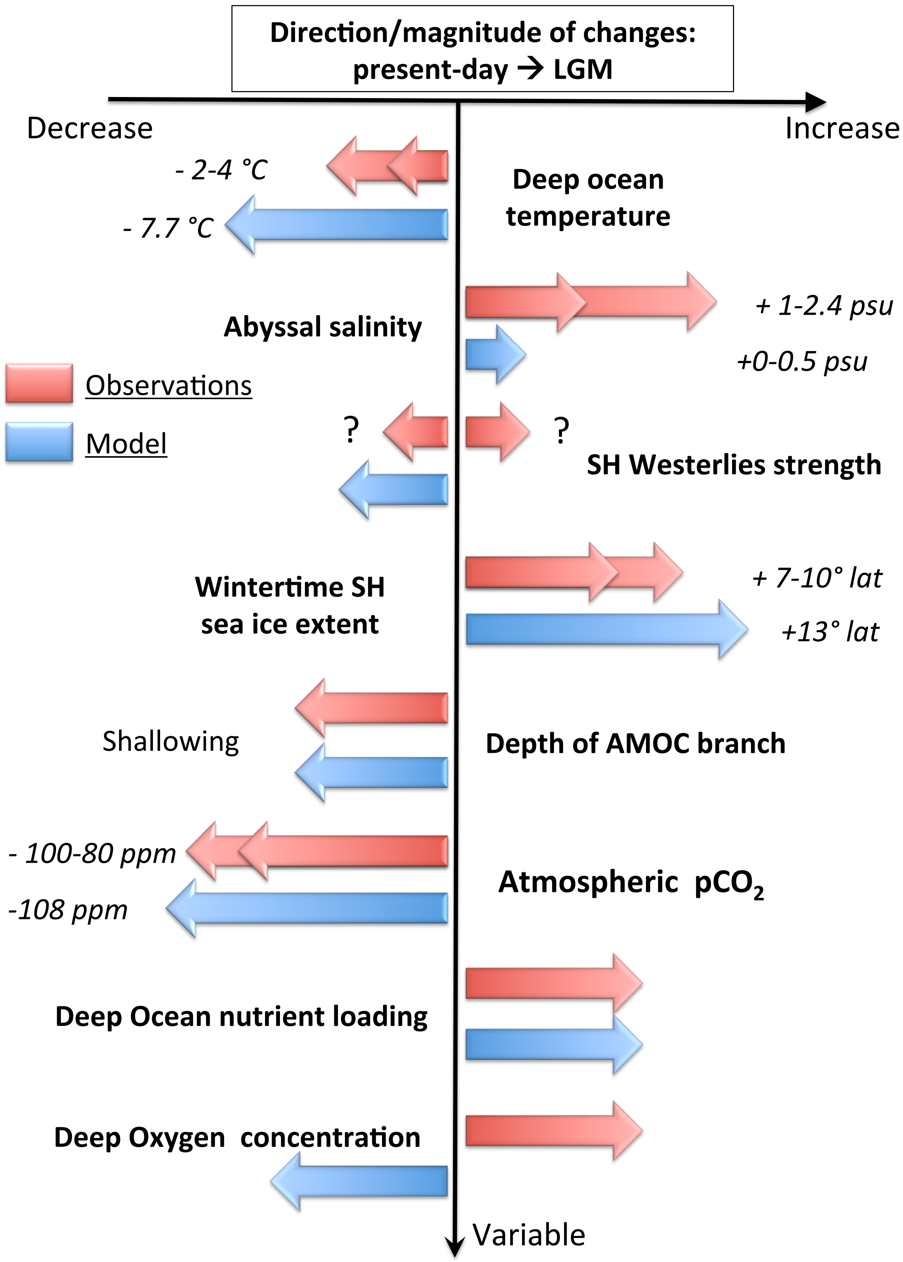

Figure 4: **Comparison of observations and simulations.** Observed changes between the LGM and present-day climates from observations (red arrows) along with the corresponding differences between the Cold and Warm states of our idealized Earth-like climate simulations (blue arrows). When possible, arrows are scaled to represent the magnitude of the changes. Double arrows for observation gives the range of uncertainties.

Linking Glacial-Interglacial states to multiple equilibria of climate

David Ferreira, John Marshall, Takamitsu Ito, David McGee

Supplementary information

1 Climate modelling framework

We use the Massachusetts Institute of Technology (MIT) GCM in a coupled ocean-atmosphere-sea ice setup [1, 2]. The model exploits an isomorphism between the ocean and atmosphere dynamics to generate an atmospheric GCM and an oceanic GCM from the same dynamic core [3]. The model uses the following (isomorphic) vertical coordinates: the rescaled pressure coordinate $p^{\star}$ for the compressible atmosphere and the rescaled height coordinate $z^{\star}$ for the Boussinesq ocean [4]. Both component models use the same cubed-sphere grid [5], at a low-resolution C24 (24×24 points per face, yielding a resolution of 3.75° at the equator). The cubed-sphere grid avoids problems associated with the converging meridian at the poles and ensures that the model dynamics at the poles are treated with as much fidelity as elsewhere. Additionally, it greatly simplifies the implementation of a conservative interface between the two GCMs [6].

The atmospheric physics is of "intermediate" complexity, based on the simplified parameterizations primitive- equation dynamics (SPEEDY) scheme [7] at low vertical resolution (five levels). This method comprises a four-band radiation scheme, a parameterization of moist convection, diagnostic clouds, and a boundary layer scheme. The 3-km-deep, flat-bottomed ocean model has 15 vertical levels, increasing from 30 m at the surface to 400 m at depth. Effects of mesoscale eddies are parameterized as an advective process [8] and an isopycnal diffusion [9], both with a transfer coefficient of 1200 m^2 s^{-1}. Convective adjustment, implemented as an enhanced vertical mixing of temperature and salinity, is used to represent ocean convection [10]. The background vertical diffusion is uniform and set to 3×10^{-5} m^2 s^{-1}. The sea ice model uses a two-and-a-half-layer thermodynamic formulation following [11]. The prognostic variables are ice fraction, snow and ice thickness, and a two-level enthalpy representation accounting for brine pockets and sea ice salinity employes an energy-conserving formulation. There are no sea ice dynamics. The land model is a simple two-layer model with prognostic temperature, liquid groundwater, and snow height. There is no continental ice. The land albedo is to set to 0.25 plus a contribution from snow, if present. The snow albedo parameterization (identical over land and sea ice) depends on the snow height, surface temperature, and snow age. Present- day orbital forcing is used and pCO_2 is set to 325 ppm in the radiative scheme. The seasonal cycle is represented but there is no diurnal cycle.

The biogeochemical component of the model consists of five tracers including Dissolved Inorganic Carbon (DIC), alkalinity, phosphate, dissolved organic phosphorus and oxygen [12]. The rates of carbon uptake and oxygen production are calculated based on the availability of phosphate and light using the Monod function. 67% of phosphate uptake turns into dissolved organic matter, and the remaining 33% sinks down as particulate organic matter. A Martin exponent of 0.90 is used for the parameterization of the vertical attenuation of sinking particles, and the dissolved organic matter decays back to inorganic nutrient and carbon with the e-folding time scale of 6 months. Remineralization of sinking organic matter and dissolved organic matter consumes oxygen with a globally uniform stoichiometric ratio, P:C:O_2 = 1:110:170. The oceanic carbon cycle is coupled to a well-mixed atmospheric reservoir of CO_2. The atmospheric CO_2 is not active radiatively active, however, and so the carbon cycle does not feed back on climate dynamics. Our focus here is on the existence of multiple states supported by the coupled dynamics, and we choose to initially treat the biogeochemical cycles as a passive component.

Finally, fluxes of momentum, freshwater, heat, salt and CO_2 are exchanged every hour (the ocean time step). Note that the present coupled ocean-sea ice-atmosphere model achieves perfect (machine accuracy) conservation of freshwater, heat, and salt during extended climate simulations [6]. This is made possible by the use of the $z^\star$ coordinate, which allows for a realistic treatment of the sea ice-ocean interface. This property is crucial to the fidelity and integrity of the coupled system.The model (or close versions of it) has been used before in process studies [13, 14, 15] with idealized configurations as well as realistic paleoclimate configurations [16].

Initial conditions for the two states. The two simulations were started from different initial conditions. The Warm state was initialized from the zonal mean state of the “Double-Drake” simulation [14] which has an ice cover at the Southern pole but not at the Northern pole. Initial conditions for the Cold state were obtained as follows: the model was again started from the zonal mean state of the ”Double-Drake” simulation but with a higher value of the ground albedo of 0.25 (typical of a rocky/desert conditions) everywhere over the continents. This albedo choice drives a global cooling of the climate system and the growth of extensive ice caps at both poles. The equilibrium state of this simulation is used as cold initial conditions to start a simulation with the exact same parameters and forcing as the Warm state (including the same ground albedo). This simulation remains in a cold climate, hence producing a second equilibrium state (the Cold state). Both the Warm and Cold solutions have been run up to equilibrium.

2 Oceanic and atmospheric energy transports

As expected from previous studies [28, 29], the total (ocean plus atmosphere) energy transport remains relatively similar between the state states, notably over regions unaffected by changes in the sea ice cover (Fig. S2, bottom). This invariance provides an interesting constraint to interpret the ocean and atmospheric energy transports.

As the Ocean Heat Transport (OHT) in the deep tropics varies little between the two states (Fig. 2, top right), the Atmospheric Heat Transport (AHT) must also remains similar. As the moist static energy contrast between the top and bottom of the troposphere is weaker in the Cold state (lower specific humidity), an intensification of the Hadley circulation in the Cold state is required to maintain the strength of the AHT at low latitudes (Fig. S3).

It is also noteworthy that the invariance of the total heat transport hides a number of compensating changes in ocean and atmospheric transports. Within the AHT, the decrease of the latent heat transport in the Cold state is largely balanced by an increase of the dry static component (not shown). Exceptions to this are found in regions of the sea ice cover change. In the band 70-50°S (ice free in the Warm state), the equatorward displacement of the storm track (with the sea ice expansion) and cooling in the Cold state result in decreases of both latent and dry static energy transports. In the northern hemisphere, in contrast, the strengthening of the storm tracks (without displacement) is associated with an intensification of the dry static energy transport which is only partially cancelled by a decreased latent heat transport.

In the ocean, the OHT undergoes a reorganization associated with changes in the deep circulation, sea-ice cover, and winds. In the Northern Hemisphere, the OHT of the small (Atlantic-like) basin decreases at all latitudes by $\sim$0.4 PW in the Cold state (Fig. S2, top), reflecting the weakening of the deep MOC. In the large basin however, the OHT in the band 0-30°N intensifies (by about 0.5 PW) in response to the strengthening of the Hadley Cell/Trade winds (i.e. strengthening of the wind-driven component of the circulation). As a results, the global OHT in the subtropics is slightly larger in the Cold state than in the Warm state (Fig. 2, top right). North of 40°N, the weakening deep MOC dominates the global OHT change which exhibits a decrease in the Cold state.

Change in the strength of the bottom cell has little impact on the OHT (the bottom cell acts on weak vertical temperature gradient and achieves little heat transport; see [30]). The OHT change in the Southern Hemisphere (0-40°S) is dominated by the weakening of upper deep cell (which transports heat northward, leading to a stronger southward transport in the Cold state, see Fig. 2). South of 40°S, changes in OHT primarily reflect the expansion of the sea ice cover that strongly damps air-sea exchanges.

3 Carbon pump analysis

3.1 Formulation

Changes in the equilibrium atmospheric CO_2 (δpCO_2) can be attributed to changes in oceanic carbon reservoirs and the total carbon inventory of the ocean-atmosphere system [17, 18]:

$$\delta pCO_2 = \left(M + \frac{V\overline{C_{ref}}}{pCO_{2,ref}B} \right)^{-1} \left(\delta I_C - V\delta\overline{C} \right), \tag{1}$$

where M is the total moles of gases in the atmosphere, V is the volume of the ocean, B is the global mean Buffer factor, and I_C is the total carbon inventory of the ocean-atmosphere system. The overline indicates the global mean. In the closed system ($\delta I_C = 0$) the change of atmospheric CO_2 is linearly related to that of the global ocean carbon storage ($V\delta\overline{C}$), which can then be decomposed into different carbon pump components:

$$\delta\overline{C} = \underbrace{\delta\overline{C^T_{sat}} + \delta\overline{C^S_{sat}}}_{solubility} + \underbrace{\delta\overline{C_{org}}}_{organic} + \underbrace{\delta\overline{C_{CaCO_3}} + \delta\overline{C^A_{sat}}}_{carbonate} + \delta\overline{C_{dis}}. \tag{2}$$

The first two terms (δC^T_{sat}, δC^S_{sat}) represent the temperature and salinity dependence of the solubility. The second group is the organic pump, measuring the cumulative effect of respiration of organic matter, which is linked to the preformed phosphate, $\delta\overline{C_{org}} = -R_{C:P}\delta\overline{P_{pre}}$. The third group is primarily controlled by the carbonate pump, including the contribution of preformed alkalinity and the cumulative remineralization of $CaCO_3$ particles. The last term is the effect of air-sea disequilibrium in regions of water mass formation, which is then transported into the interior ocean.

Combining Eqs. (1) and (2), changes in atmospheric CO_2 can be attributed to different mechanisms. The constant of proportionality depends on the size of the oceanic and atmospheric carbon reservoir and the global mean buffer factor. As a rule of thumb, $1\mu M$ increase in the ocean carbon storage ($\delta\overline{C}$) leads to approximately 1 ppm decrease in the atmospheric CO_2.

To calculate the individual effects, we follow the methodology of [18]. The diagnostic calculation is based on the parameters and inventories used in our model. C_{org} is determined based on the apparent oxygen utilization. Preformed alkalinity is estimated using multiple linear regression at the surface, which allows us to calculate the regenerated alkalinity and the carbonate pump, C_{CaCO_3}. Preformed DIC (C_{pre}) is determined by subtracting organic and carbonate pumps (C_{org}, C_{CaCO_3}) from the total DIC. Saturation DIC concentration C_{sat} is calculated from thermodynamic equilibrium relations, and the air-sea disequilibrium component C_{dis} is determined as a residual between C_{pre} and C_{sat}.

Theoretically, preformed alkalinity is set when the water was last in contact with the mixed layer, and it has to be empirically determined. In practice, multiple linear regression can be used to estimate the preformed alkalinity for each climate states using salinity and preformed phosphorus as the input parameters. Saturation DIC concentration C_{sat} depends on temperature, salinity, alkalinity and pCO_2. The properties of Csat and Cdis are determined at the time of water mass formation, and their distributions correlates with hydrographic structures. Csat mainly reflects the temperature of water masses. Positive values of Cdis in the AABW-like water masses indicate that the surface CO_2 is supersaturated in the deep water formation region of the southern high latitudes. The global mean buffer factor of 12 is used in this study. Carbon pumps and their changes between the two climate states are shown in Table 1.

3.2 Discussion

The reduction of the oceanic carbon storage C_{org} (an atmospheric CO_2 increase of +52 ppm; see Table 1) is associated with a weakening of Antarctic productivity and an increase in the preformed phosphorus of the AABW-like water. As a constant $CaCO_3$ rain ratio is assumed in our model, the carbonate pump C_{CaCO3} weakens along with the organic pump C_{org}, leading to an additional ocean carbon storage due to an increase in the preformed alkalinity. The net effect of the weakened carbonate pump decreases the atmospheric CO_2 by 16 ppm.

If the effect of glacial iron fertilization were to be included in our simulations, the simulated atmospheric pCO_2 may further decrease by a few tens of ppm [19, 20]. The reconstruction of preformed nutrient content for the glacial AABW is still elusive and is under intense research [21, 22, 23, 24]. While the mechanistic link between glacial-interglacial changes in Subantarctic productivity and Antarctic preformed phosphorus is not fully understood, the glacial deep Pacific contained a lower level of dissolved O_2 [25, 26] indicating that the iron fertilization of the Subantarctic likely influenced the Antarctic preformed phosphate and the amount of regenerated nutrients in deep waters.

In reality the reduction of land biomass likely added approximately 500 PgC to the ocean-atmosphere system during recent glacial periods, leading to an atmospheric CO_2 increase of $\sim$15 ppm [27]. Furthermore, the effect of land ice volume raises the mean salinity of the seawater, raising atmospheric CO_2 by about $\sim$7 ppm[27]. These effects are not accounted for in our study, and so the transfer of carbon to the deep water has to be the equivalent of about -102 ppm in order to reproduce the observed glacial CO_2

drawdown of -80 ppm.

While the dissolution of carbonate sediment is not resolved in our model, the elevated level of DIC in the bottom water makes it more corrosive to sedimentary $CaCO_3$, and the resultant carbonate dissolution would further decrease the atmospheric CO_2 in the Cold state. Additional CO_2 drawdown is expected due to the effect of increased dust deposition and the $CaCO_3$ compensation triggered by the increased bottom water DIC[22].

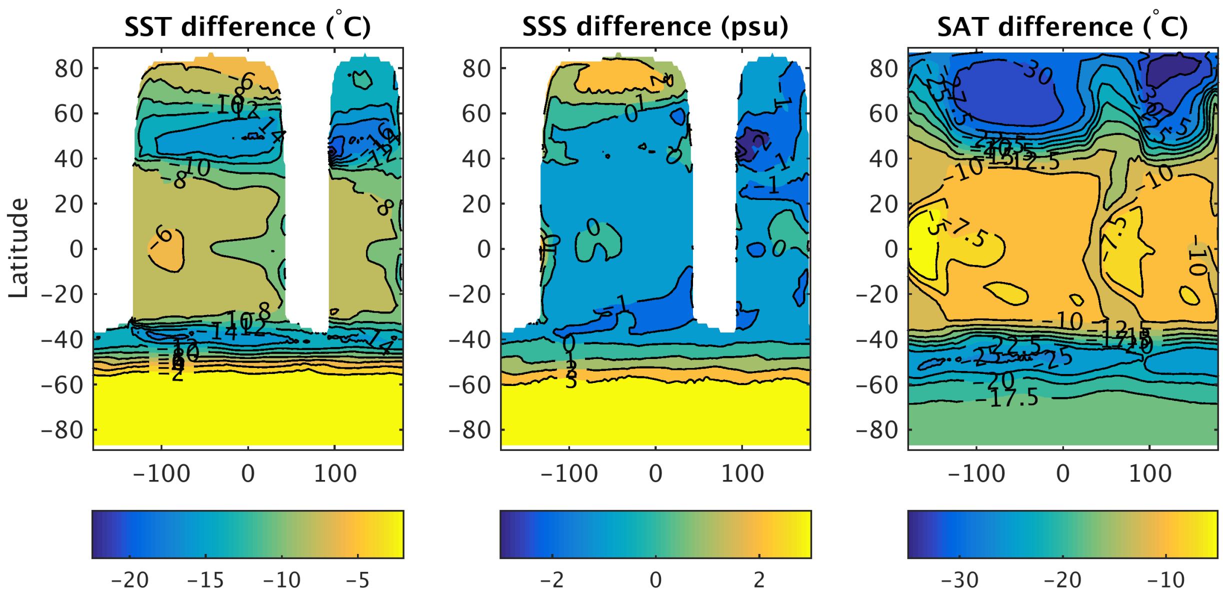

FIG. S1: Differences in annual mean Sea Surface Temperature (°C), Sea surface Salinity (psu), and Surface Air Temperature (°C) between the Cold and Warn states. For SST, minimum changes are found in the Southern Hemisphere, south of 60°S, where sea ice is present in both states (the slight cooling in that region is due to a small salinity increase and decrease of the freezing point). Maximum changes are found in locations that experienced change in sea ice cover. The equatorial region shows a minimum in temperature drop. The pattern of SAT change bares many similarities with that of SST. Note the minimum cooling are over the equatorial continent, while ice covered regions of the SH in the Warm state do exhibit a large cooling.

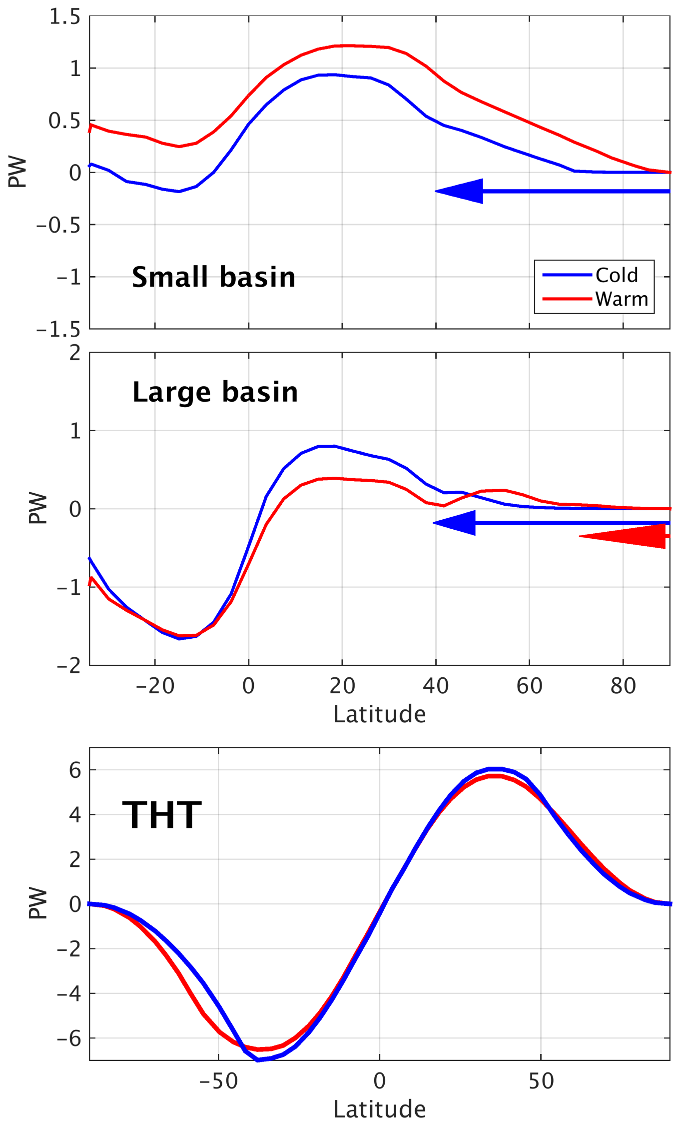

Fig. S2: Heat transport (in PW = 10^{15} W) in the Warm (red) and Cold (blue) states: (top) Small basin OHT, (middle) Large Basin OHT, and (bottom) total (ocean plus atmosphere) energy transports. The arrows denote the corresponding sea ice extents. The length of the arrow head indicate the seasonal range.

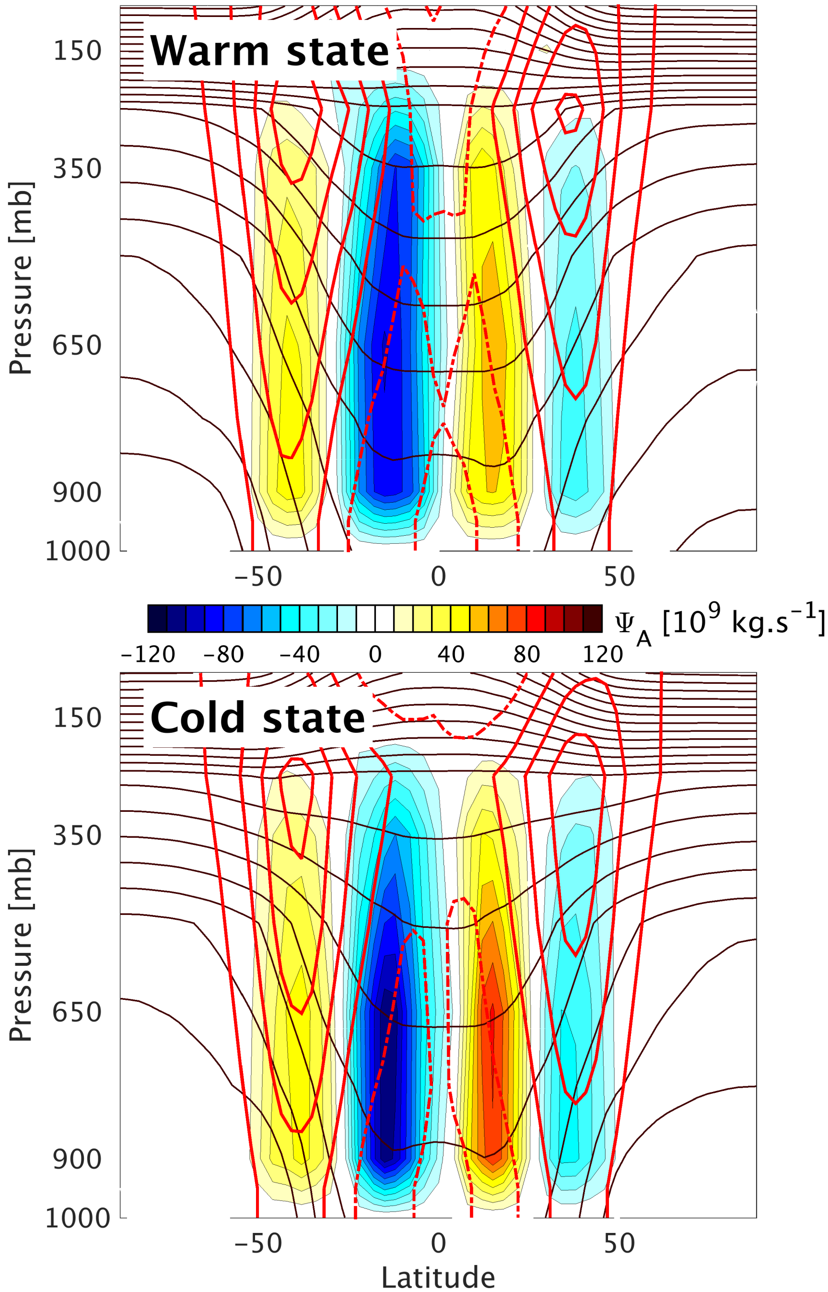

Fig. S3: **Atmospheric state of the multiple equilibria:** Overturning streamfunction (color shading, contour interval of $10{\times}10^9$ kg s^{-1}, the zero contour is omitted), potential temperature (black solid lines with a 10 K contour interval) and zonal-mean zonal winds (red lines, contours at ±5, ±15, ±25 m s^{-1} ..., solid and dashed lines denote westerly and easterly winds, respectively). The Warm state is shown in the top panel and the Cold state in the bottom panel.

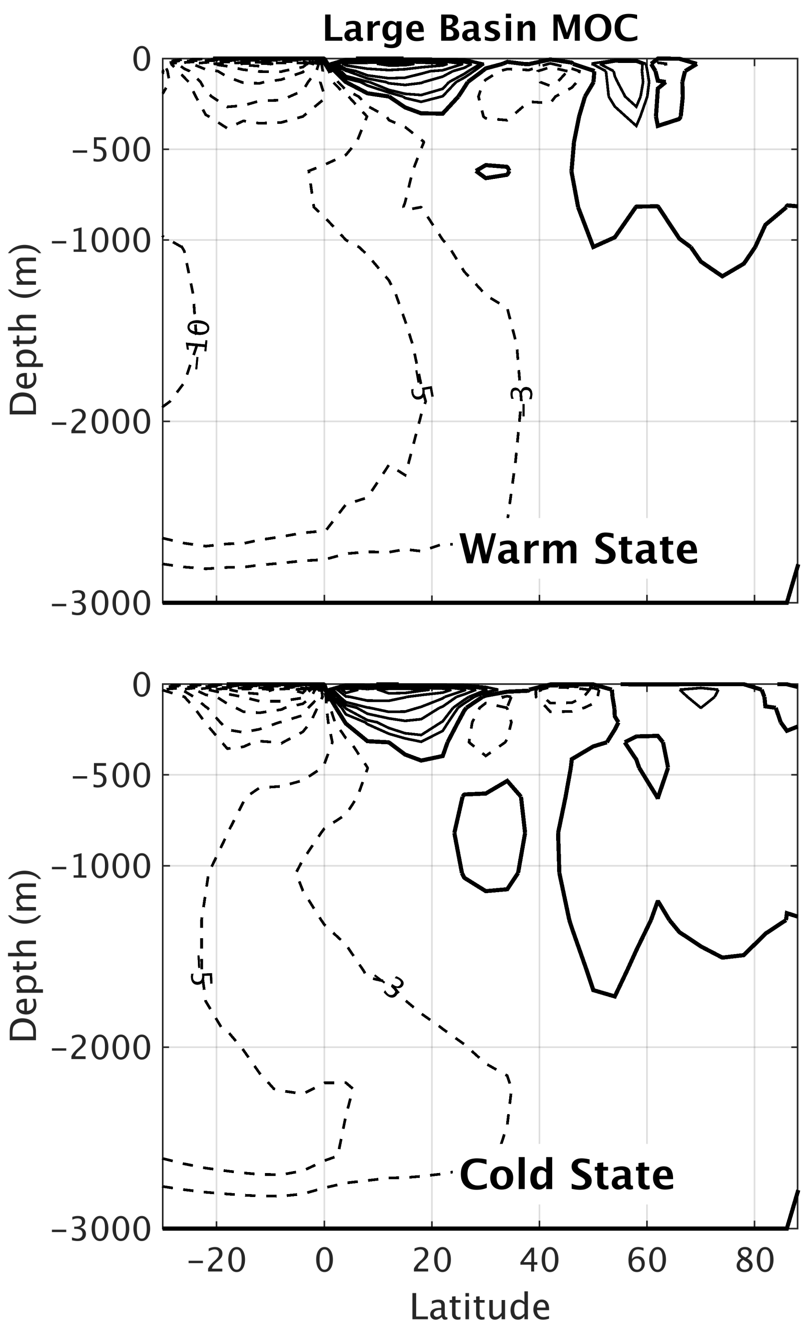

Fig. S4: Meridional Overturning Circulation (in Sv) in the large basin for the Warm state (top) and Cold state (bottom). Solid and dashed lines correspond to clockwise and counter-clockwise circulations, respectively. The zero contour is shown with a thick line.

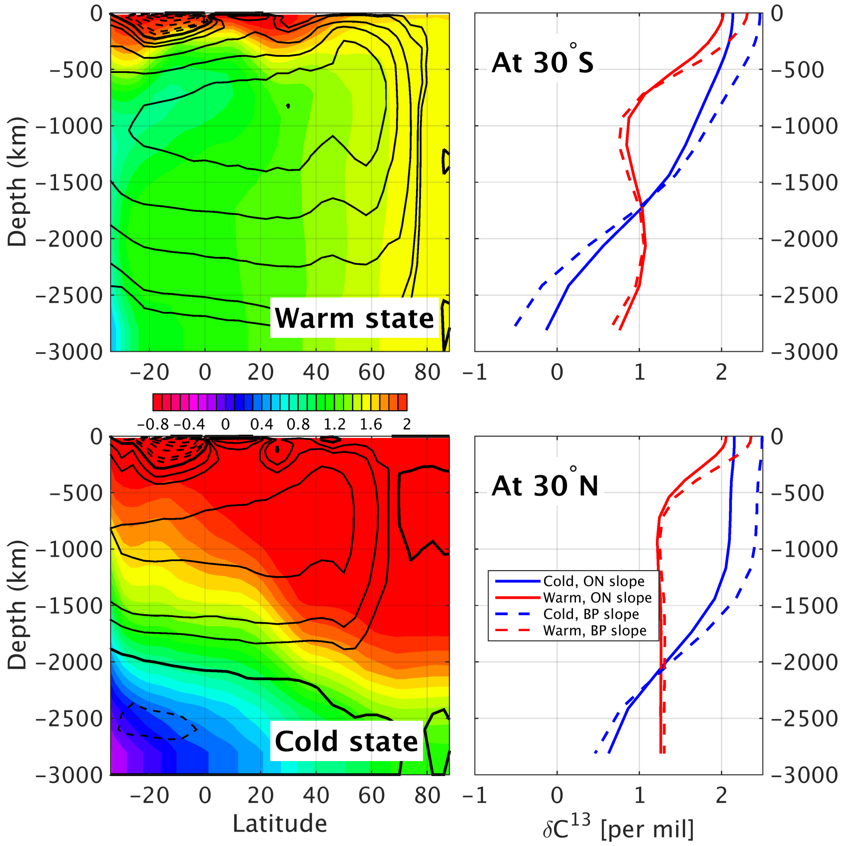

FIG. S5: Reconstructed distributions of δC^{13} (in ‰) in the Small basin, estimated from the quasi-linear relationship between phosphate and δC^{13} observed in the present-day ocean. Two linear fits by [31] (BP) and [32] (ON) are considered. Note that both estimates correct for the invasion of the isotopically-light anthropogenic carbon dioxide. (Right) Depth-latitude distribution of δC^{13} based on the ON fit for the Warm (top) and Cold (bottom) states. The MOC contours are superimposed. (Left) Profiles at (top) 30°S and (bottom) 30°N highlighting the uncertainties associated with the choice of linear fit, ON in solid line and BP in dashed lines. Changes in the estimated δC^{13} distribution between the states is much larger than the uncertainties associated with the linear fit. The patterns and magnitude of the reconstructed δC^{13} distributions are in reasonable agreement with those inferred for the present-day ocean and LGM ocean.

References

[1] Marshall, J., Adcroft, A., Hill, C., Perelman, L. & Heisey, C. A finite-volume, incompressible navier stokes model for studies of the ocean on parallel computers. *J. Geophys. Res.* **102**, 5753–5766 (1997).

[2] Marshall, J., Hill, C., Perelman, L. & Adcroft, A. Hydrostatic, quasi-hydrostatic, and nonhydrostatic ocean modeling. *J. Geophys. Res.* **102**, 5733–5752 (1997).

[3] Marshall, J., Adcroft, A., Campin, J.-M., Hill, C. & White, A. Atmosphere-ocean modeling exploiting fluid isomorphisms. *Mon. Wea. Rev.* **132**, 2882–2894 (2004).

[4] Adcroft, A. & Campin, J.-M. Re-scaled height coordinates for accurate representation of free-surface flows in ocean circulation models. *Ocean Modell.* **7**, 269–284 (2004).

[5] Adcroft, A., Campin, J., Hill, C. & Marshall, J. Implementation of an atmosphere-ocean general circulation model on the expanded spherical cube. *Mon. Wea. Rev.* **132**, 2845–2863 (2004).

[6] Campin, J.-M., Marshall, J. & Ferreira, D. Sea ice-ocean coupling using a rescaled vertical coordinate $z^{\star}$. *Ocean Modell.* **24**, 1–14 (2008).

[7] Molteni, F. Atmospheric simulations using a GCM with simplified physical parametrizations. I: model climatology and variability in multi-decadal experiments. *Climate Dyn.* **64**, 175–191 (2003).

[8] Gent, P. R. & McWilliams, J. C. Isopycnic mixing in ocean circulation models. *J. Phys. Oceanogr.* **20**, 150–155 (1990).

[9] Redi, M. H. Oceanic isopycnal mixing by coordinate rotation. *J. Phys. Oceanogr.* **12**, 1154–1158 (1982).

[10] Klinger, B. A., Marshall, J. & Send, U. Representation of convective plumes by vertical adjustment. *J. Geophys. Res.* **C8**, 18,175–18,182 (1996).

[11] Winton, M. A reformulated three-layer sea ice model. *J. Atmos. Oceanic Technol.* **17**, 525–531 (2000).

[12] Dutkiewicz, S., Heimbach, P., Follows, M. J. & Marshall, J. C. Controls on ocean productivity and air-sea carbon flux: an adjoint model sensitivity study. *Geophys. Res. Lett.* **33**, L02603 (2006).

[13] Marshall, J., Ferreira, D., Campin, J. & Enderton, D. Mean climate and variability of the atmosphere and ocean on an aquaplanet. *J. Atmos. Sci.* **64**, 4270–4286 (2007).

[14] Ferreira, D., Marshall, J. & Campin, J.-M. Localization of deep water formation: role of atmospheric moisture transport and geometrical constraints on ocean circulation. *J. Climate* **23**, 1456–1476 (2010).

[15] Ferreira, D., Marshall, J. & Rose, B. Climate determinism revisited: multiple equilibria in a complex climate model. *J. Climate* **24**, 992–1012 (2011).

[16] Pohl, A., Y.Donnadieu, Hir, G. L. & Ferreira, D. The climatic significance of late ordovician-early silurian black shales. *Paleoceanography* **Submitted** (2017).

[17] Ito, T. & Follows, M. J. Preformed phosphate, soft tissue pump and atmospheric CO_2. *J. Mar. Res.* **63**, 813–839 (2005).

[18] Ito, T. & Follows, M. J. Air-sea disequilibrium of carbon dioxide enhances the biological carbon sequestration in the southern ocean. *Glob. Biogeochem. Cy.* **27**, 1–10 (2013).

[19] Bopp, L., Kohfeld, K. E., Le Quéré, C. & Aumont, O. Dust impact on marine biota and atmospheric co2 during glacial periods. *Paleoceanography* **18**, 1046 (2003).

[20] Parekh, P., Dutkiewicz, S., Follows, M. J. & Ito, T. Atmospheric carbon dioxide in a less dusty world. *Geophys. Res. Lett.* **33**, L03610 (2006).

[21] Francois, R. F. & et al. Water column stratification in the southern ocean contributed to the lowering of glacial atmospheric co2. *Nature* **389**, 929–935 (1997).

[22] Toggweiler, J. R. Variations in atmospheric co2 driven by ventilation of the ocean's deepest water. *Paleoceanography* **14**, 571–588 (1999).

[23] Sigman, D. M., Hain, M. P. & Haugh, G. H. The polar ocean and glacial cycles in atmospheric co2 concentration. *Nature* **466**, 47–55 (2010).

[24] Watson, A. J., Vallis, G. K. & Nikurashin, M. Southern ocean buoyancy forcing of ocean ventilation and glacial atmospheric CO_2. *Nature Geoscience* **8**, 861–864 (2015).

[25] Galbraith, E. D. *et al.* Carbon dioxide release from the north pacific abyss during the last deglaciation. *Nature* **449**, 890–893 (2007).

[26] Jaccard, S. L. *et al.* Subarctic pacific evidence for a glacial deepening of the oceanic respired carbon pool. *Earth and Planet. Sci. Lett.* **277**, 156–165 (2009).

[27] Sigman, D. M. & Boyle, E. A. Glacial/interglacial variations in atmospheric carbon dioxide. *Nature* **407**, 859–869 (2000).

[28] Stone, P. H. Constraints on dynamical transports of energy on a spherical planet. *Dyn. Atmos. Oceans* **2**, 123–139 (1978).

[29] Enderton, D. & Marshall, J. Explorations of atmosphere-ocean-ice climates on an aqua-planet and their meridional energy transports. *J. Atmos. Sci.* **66**, 1593–1611 (2009).

[30] Ferrari, R. & Ferreira, D. What processes drive the ocean heat transport? *Ocean Modell.* **38**, 171–186 (2011).

[31] Broecker, W. S. & Peng, T.-H. *Tracers in the Sea* (Lamont-Doherty Geological Observatory, Columbia University, 1982).

[32] Olsen, A. & Ninnemann, U. Large δ^{13}C gradients in the preindustrial north atlantic revealed. *Science* **330**, 658–659 (2010).